ADVANCED OPTICAL MATERIALS

Supporting Information

for *Adv. Optical Mater.*, DOI 10.1002/adom.202400803

Large Mid-Infrared Magneto-Optic Response from Doped Cadmium Oxide at Its Epsilon-Near-Zero Frequency

*Jonathon R. Schrecengost, Angela J. Cleri, Maxwell J. Tolchin, Ramya Mohan, John P. Murphy, Sara Adamkovic, Alex J. Grede, Mario V. Imperatore, Patrick E. Hopkins, Jon-Paul Maria and Noel C. Giebink**

Supplementary Material

Large Mid-infrared Magneto-Optic Response from Doped Cadmium Oxide at its Epsilon-Near-Zero Frequency

Jonathon R. Schrecengost, Angela J. Cleri, Maxwell J. Tolchin, Ramya Mohan, John P. Murphy, Sara Adamkovic, Alex J. Grede, Mario V. Imperatore, Patrick E. Hopkins, Jon-Paul Maria, Noel C. Giebink.

S1. Approximate expressions

As described in Ref. [1], various Taylor series approximations can be used to simplify the exact solution for Θ and F in the 'transparent region' where ε'' is small:

$$\Theta = -\frac{\omega}{2c}\frac{g'}{\sqrt{\varepsilon'_{xx}}} \tag{S1}$$

$$F = \frac{|g'|}{2(\varepsilon''_{xx} + g'')} \tag{S2}$$

In Ref. [2], an explicit form for Θ is derived in the transparent region:

$$\Theta = \frac{\mu_0 N q^3 \lambda^2}{8\pi^2 m^{*2} n c}, \tag{S3}$$

where μ_0 is the permeability of free space, c is the speed of light and all of the other parameters retain the same meaning as in the main text. In this case, $\alpha = \mu_0 N q^2 \lambda^2 / 4\pi^2 m^* n \tau c$, where τ is the scattering time in the Drude model, and thus the figure of merit is simply $F = \mu_{opt}/2$. Figure S1 compares each of these approximations with the exact solution calculated numerically.

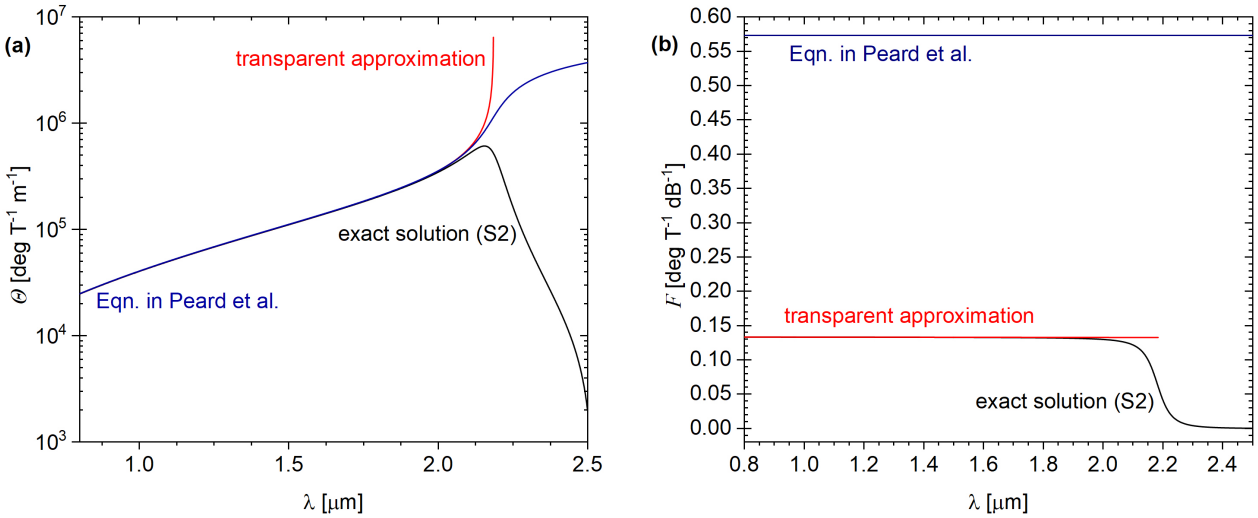

Figure S1. Comparison of the transparent approximations used in Ref. [1] and [2] with the exact solutions for **(a)** the Verdet constant and **(b)** the MO rotational figure of merit in sample S2. Both approximations show agree well with the exact solution for Θ below λ_{ENZ}, but break down near and above λ_{ENZ}.

S2. Additional samples and full Faraday rotation data set

name	dopant	ENZ (nm)	N (cm^{-3})	μ_{opt} ($cm^2 \cdot V^{-1} \cdot s^{-1}$)	m^* (m_e)	ε_∞	substrate	thickness (nm)
S9	Gd	2247	$2.65 \cdot 10^{20}$	201	0.222	5.3	sapphire	240
S10	Gd	2256	$2.65 \cdot 10^{20}$	186	0.225	5.3	sapphire	490
S11	Gd	2235	$2.68 \cdot 10^{20}$	187	0.225	5.3	sapphire	2100
S12	Gd	2391	$2.3 \cdot 10^{20}$	200	0.221	5.3	BK7	630
S13	Gd	2346	$2.4 \cdot 10^{20}$	175	0.222	5.3	Si	550
S14	Gd	2186	$2.8 \cdot 10^{20}$	200	0.225	5.3	sapphire	1000

Table S1. Additional films fabricated & measured with similar target Drude parameters, but different thicknesses and substrates. The substrates are 430 µm thick c-plane sapphire, 500 µm thick BK7 glass, 280 µm thick <100> undoped Si, and 1 mm thick soda lime glass in the case of the ITO sample.

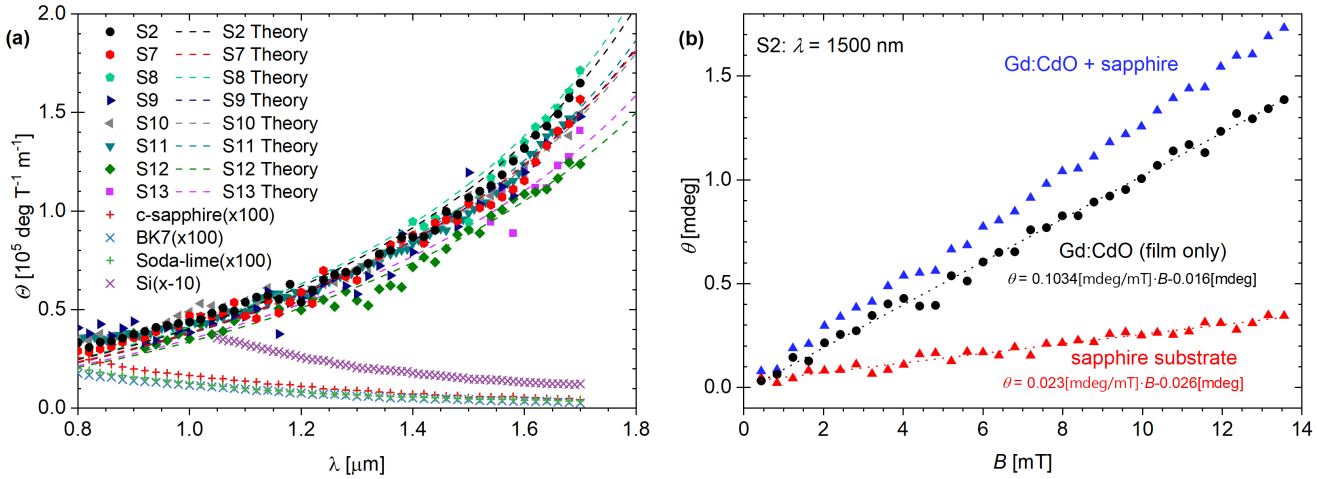

Figure S2. (a) The Verdet constant measured from 0.8–1.7µm for a variety of doped CdO films with similar Drude parameters but different dopants (S2 vs. S7), thicknesses (S2 vs. S9-11), and substrates (S2 vs. S8, S12, S13). The Verdet constant of doped CdO films is found to be independent of dopant, thickness, and substrate as long as the films have similar Drude parameters. Also shown are the measured Verdet constants of all substrates used, which are scaled as indicated in the legend in order to be seen in this plot. **(b)** Example Faraday rotation per pass vs. magnetic field strength for a doped CdO film on sapphire (S2) and a bare sapphire substrate at λ=1500 nm. Subtracting the latter from the former yields the rotation for the film by itself. Linear fits to each data set yield the slope, which in turn is divided by the film or substrate thickness to calculate the Verdet constant.

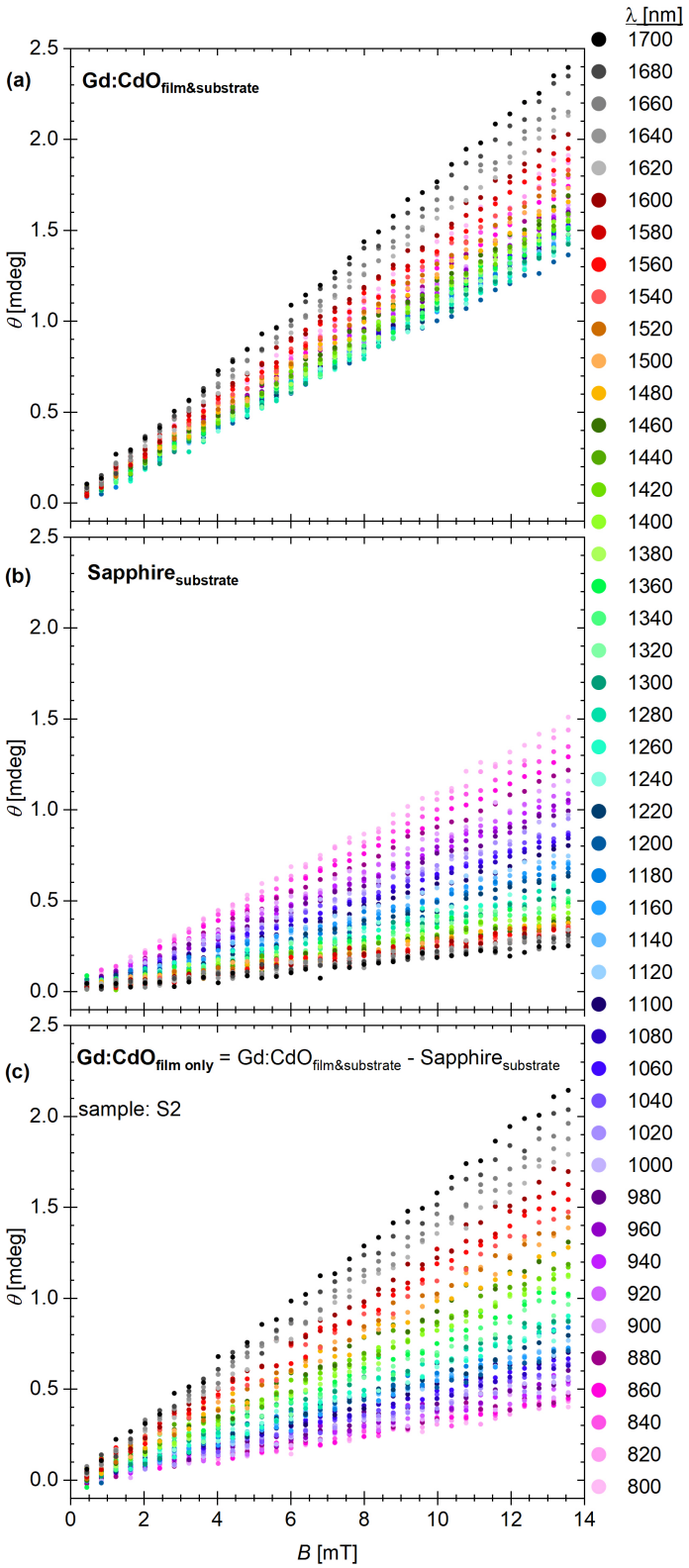

Figure S3. Faraday rotation data for all of the wavelengths measured. The rotation per pass vs. magnetic field is shown in **(a)** for a Gd:CdO film on its sapphire substrate (sample S2), **(b)** the

bare sapphire substrate, and **(c)** the result for the Gd:CdO film by itself after subtracting the substrate data in (b) from the substrate+film data in (a).

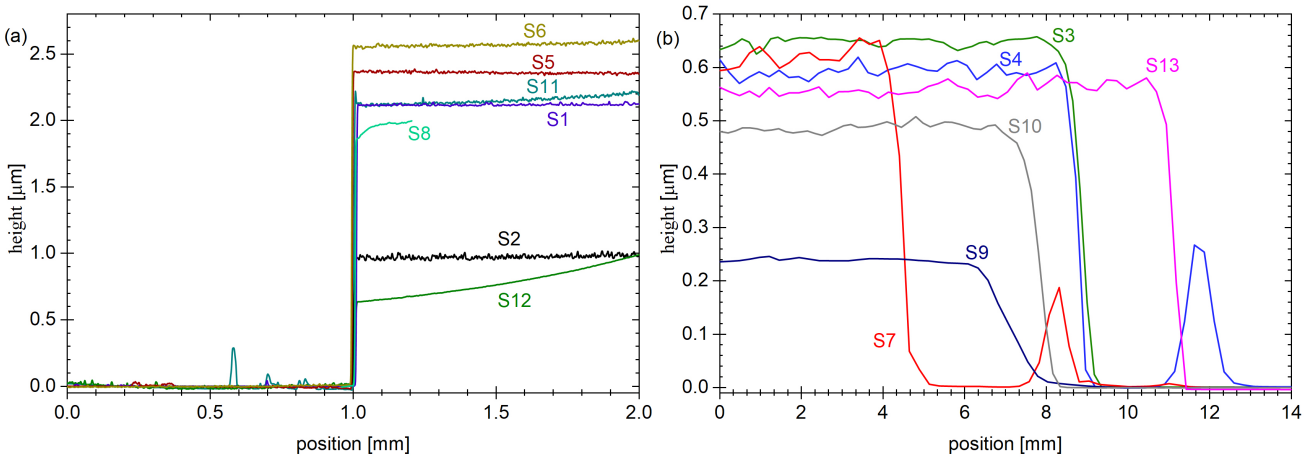

Figure S4. (a) Mechanical profilometry and **(b)** AFM scans over the step edge of each film on its substrate. The thickness of each film was extracted, listed in Table 1 and Table S1, and used in the Verdet constant calculations.

S3. Faraday ellipticity

Figure S5(a) shows the Faraday ellipticity obtained from Eqn. (6) in the main text, which is small at wavelengths below λ_{ENZ} and thus good for Faraday rotation applications that require linear polarization to be maintained (see Supplementary Figure S7(c) below). In contrast to the near-dispersionless rotational MO figure of merit that decays as the Verdet constant nears its peak (Figure 3 in the main text), the analogous elliptical MO figure of merit (i.e. Ψ/α_{max}) shown in Figure S5(b) peaks at λ_{ENZ} where Ψ is largest. Given that this peak increases linearly with μ_{opt} (Supplementary Figure S7(d,e)), CdO may be particularly useful for applications that exploit ellipticity, such as magnetic field-tunable linear ↔ circular polarization filters.

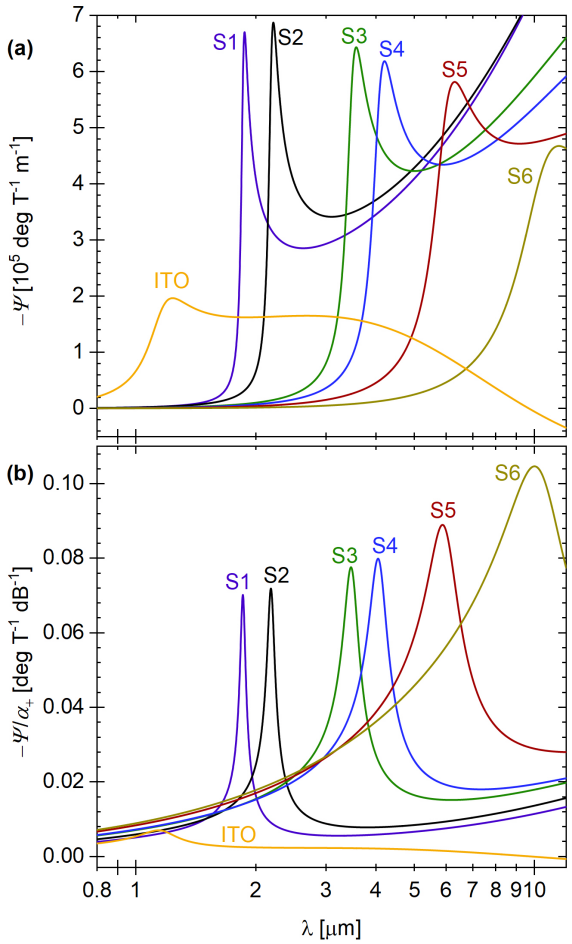

Figure S5. (a) Specific Faraday ellipticity calculated using Eqn. (6). **(b)** The elliptical MO figure of merit (equal to Eqn. (6) divided by α_{max}) peaks near the ENZ wavelength.

S4. Impact of Drude parameters on MO response

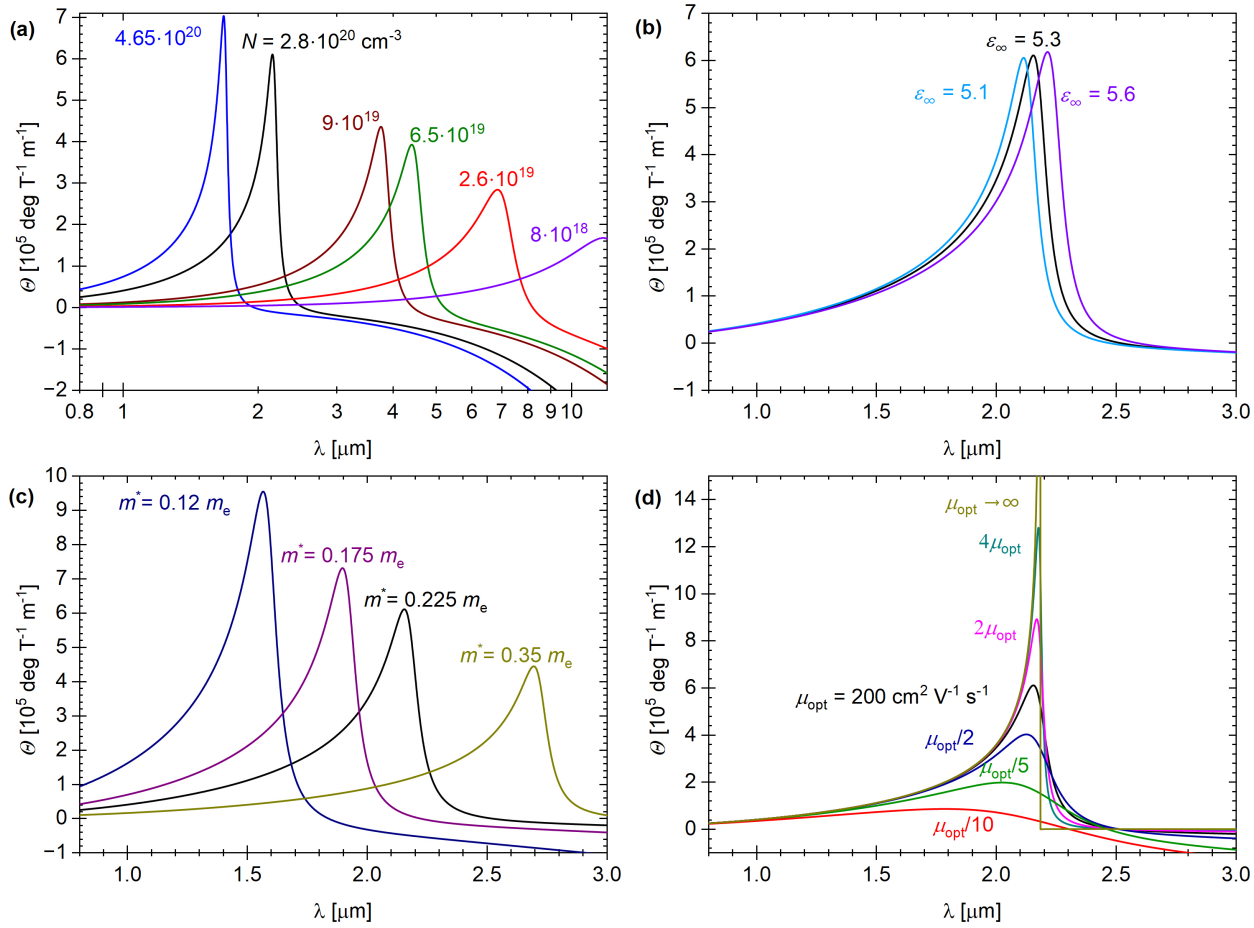

Figure S6. Varying each of the four parameters N, μ_{opt}, m^* and ε_∞ *in isolation* to study their respective effects on the Verdet constant. The lines in black represent a common set of parameters between all plots with $N = 2.8{\cdot}10^{20}$ cm^{-3}, $\mu_{opt} = 200$ cm$^2{\cdot}$V$^{-1}{\cdot}$s^{-1}, $m^* = 0.225{\cdot}m_e$, and $\varepsilon_\infty = 5.3$. Over their range of possible values for CdO [3] the trend can be studied for **(a)** carrier concentration, **(b)** high frequency permittivity, **(c)** electron effective mass, and **(d)** mobility.

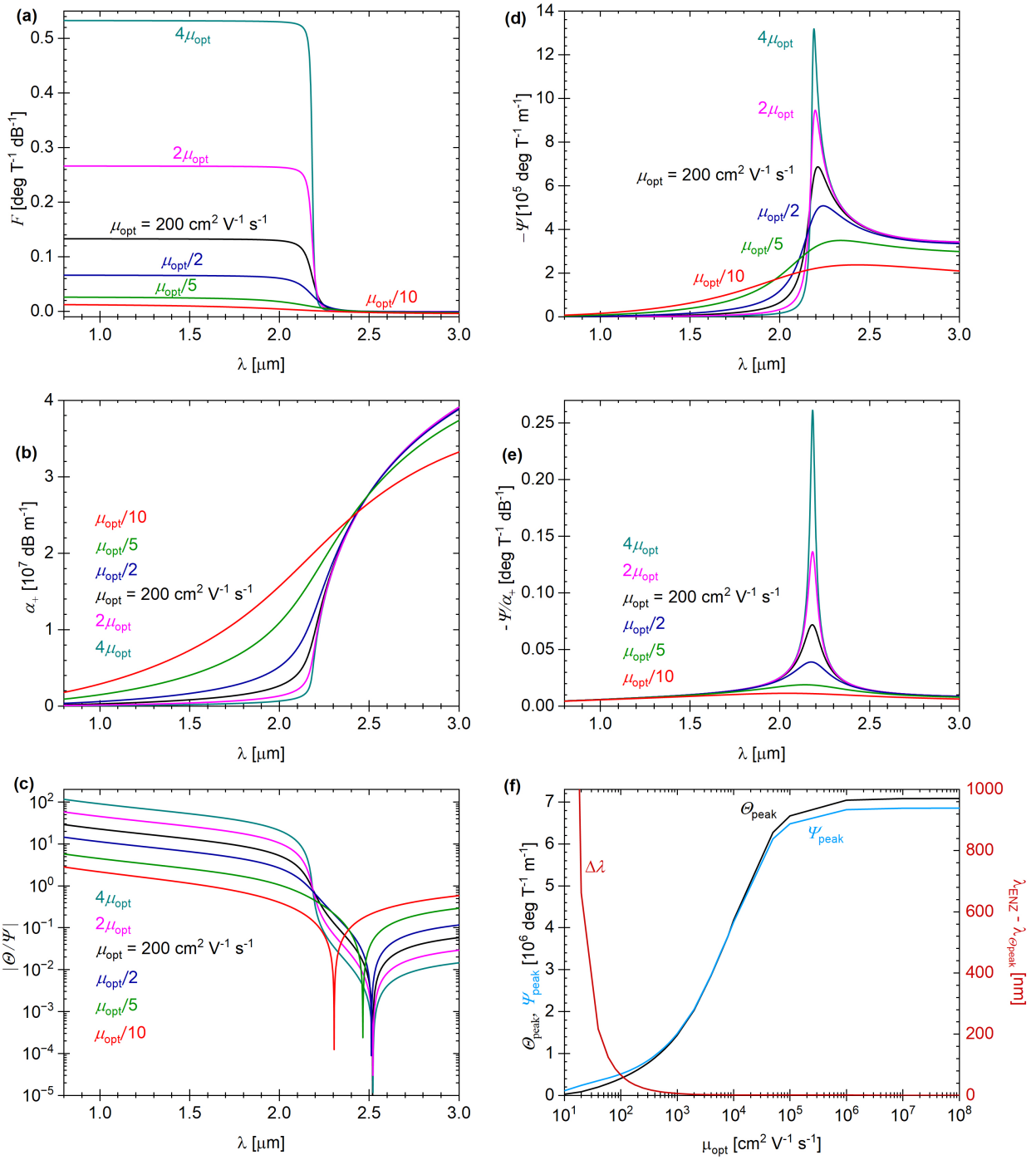

Figure S7. Effects of mobility on **(a)** rotational MO figure of merit, **(b)** absorption coefficient α [dB m^{-1}] = $4.3 \cdot \alpha$[m^{-1}], **(c)** degrees of Faraday rotation per degree of Faraday ellipticity (Θ/Ψ), **(d)** specific Faraday ellipticity, and **(e)** elliptical MO figure of merit. The lines in black represent a common set of parameters between all plots with $N = 2.8 \cdot 10^{20}$ cm^{-3}, $\mu_{opt} = 200$ cm^2·V^{-1}·s^{-1}, $m^* = 0.225 \cdot m_e$, $\varepsilon_\infty = 5.3$. **(f)** Peak Verdet constant and specific Faraday ellipticity values vs. μ_{opt}, which both saturate as $\gamma \to 0$ (simulated at $B = 1$T; when $\gamma \to 0$, ω_c can slightly limit Θ_{max}). The right axis depicts the blueshift between the Θ_{peak} and λ_{ENZ}, which results only for low mobilities.

Figure S7f suggests that the peak values of Θ and Ψ increase with μ_{opt}, but interestingly they plateau at μ_{opt} ~10^5 cm^2 V^{-1} s^{-1}, yielding a maximum theoretical value of ~$7 \cdot 10^6$ deg T^{-1} m^{-1} for a sample with the doping concentration of sample S2. Moreover, the largest gains occur in the $10^3 < \mu_{opt} < 10^4$, motivating future work to achieve mobilities in such a range, possibly through a combination of lowering temperature [4], deploying hyperbolic stacks [5] [6], improved growth methods [7], or different materials combinations [7]. Additionally, such an increase in μ_{opt} would nearly eliminate loss from attenuation and provide an excellent material for bulk MO applications.

S5. High-field MO polarimeter

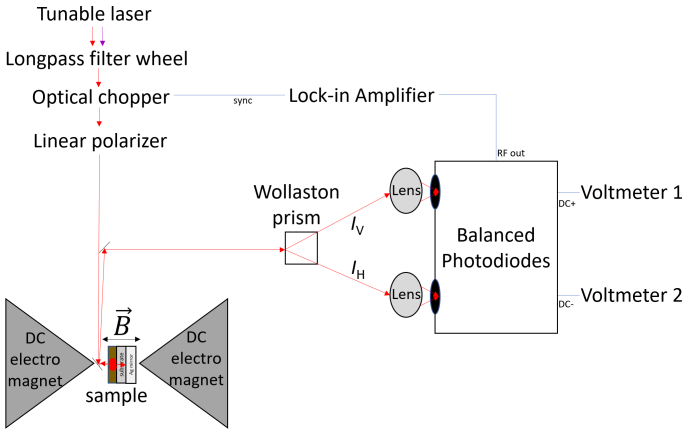

Figure S8. Magneto-optic polarimeter used to measure Faraday rotation at fields up to 3 T. This system was only used to measure sample S14 (a witness of S2), resulting in the data shown in Fig. 5(a) of the main text. **(b)** Rotation vs high magnetic field strength of S14, showing the Faraday rotation of doped CdO remains linear even at high magnetic field strengths. The magnitude of the Verdet constant of S14 was found to be in agreement with that of S2.

S6. Transmittance and reflectance spectra

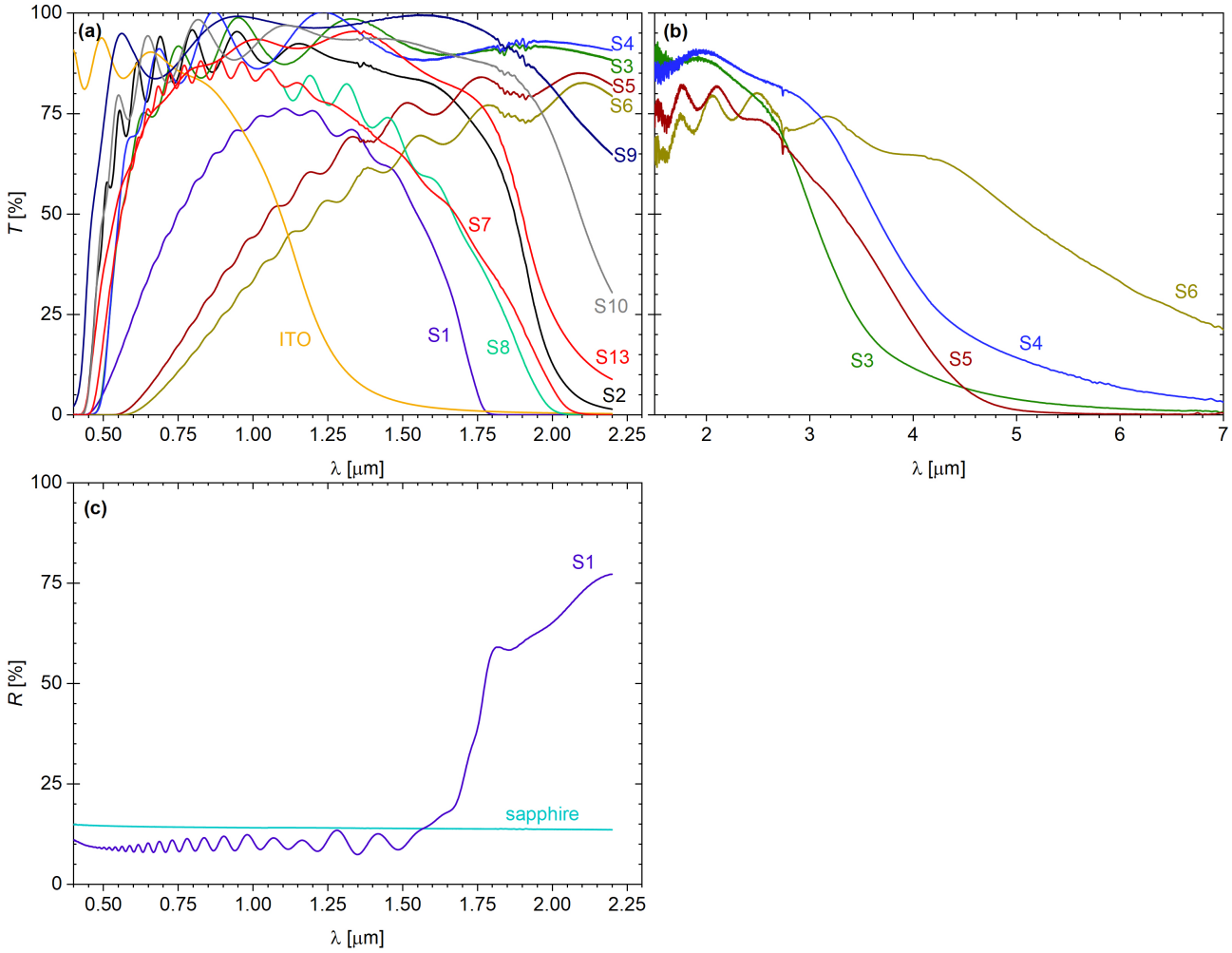

Figure S9. (a) UV-Vis-NIR and **(b)** FTIR transmittance taken at normal incidence referenced to the transmittance of the bare substrate in each case. **(c)** The rapid decrease in transmitance near ENZ is primarily due to the increase in reflectivity as shown in (c) for S1 at a 6 degree incidence angle.

S7. Characterization of Gd-doped CdO

While In:CdO thin films have been characterized extensively [3] [4] [5] [6] [8], this work is the first demonstration of Gd:CdO. Transport properties were quantified by Hall Effect measurements (see Methods) in ~100 nm films with varying Gd content defined by controlling RF power for the Gd magnetron (Figure S10a). Carrier concentration and mobility of Gd:CdO was found to be in the same range as previously explored dopants including In (Figure S10b).

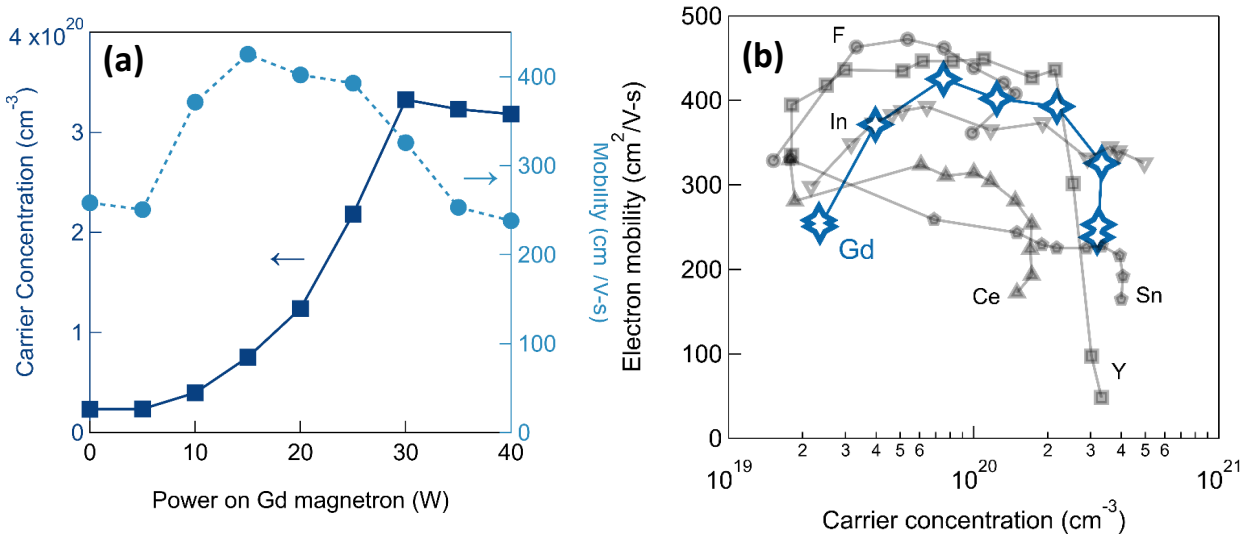

Figure S10. (a) Carrier concentration and mobility as a function of RF power on Gd magnetron. **(b)** Carrier concentration vs. mobility for Gd:CdO (blue) compared to previously explore donor dopants (gray).

The percentage of dopant atoms to total atoms in each film was determined by calibrating the dopant flux as follows. In the case of sample S1, for example, we deposited indium oxide (In_2O_3) by single cathode RF sputtering and calculated an In concentration analogous to the composition expected in In:CdO. The deposition conditions (i.e., temperature, pressure, gas flow, etc.) to fabricate an In_2O_3 thin film on c-Al_2O_3 substrate were identical to those used for the co-sputtering of In and CdO in sample S1. X-ray reflectivity measurements determined the In_2O_3 to be 21 nm thick with a relative density of 6.57 g/cm^{-3}. These physical properties were then used to

calculate the In flux of 8.05 x 10^{14} atoms/min. Using this flux, we determined the expected In concentration in sample S1 as 2.16 x 10^{21} cm^{-3}. Thus, given the measured electron concentration of 4.65 x 10^{20} cm^{-3} in sample S1, roughly 22% of the In atoms incorporated into the lattice are thermally activated and contribute to the carrier concentration. Given the density (~8.15 g cm^{-3}) and molar mass (128.4 g mol^{-1}) of CdO, the number density of atoms in the CdO crystal is ~$7.6 \cdot 10^{22}$ atoms/cm^3, meaning that In accounts for roughly 2.8% of the total atoms in the highest doped film. A similar calculation approach was used to estimate the Gd fraction in sample S2 as 1.8% of the atoms in the film.

X-ray diffraction was used to assess crystal quality of the films discussed in this work, most of which are grown on (001) (i.e. *c*-plane) Al_2O_3. Epitaxial CdO growth on *c*-Al_2O_3 would result in the (001) CdO plane tilting 23.5-degrees to sapphire (001) with a tilt direction parallel to sapphire <100>, corresponding to a (025) CdO plane parallel to the sapphire basal plane. Because of this, epitaxial CdO reflections would be visible only in asymmetric of skew-symmetric scans. However, CdO (111) peaks occur in films discussed in this report, which are visible in symmetric θ-2θ scans and increase in intensity with increasing film thickness (Figure S11a). The presence of these peaks indicates that films do not grow epitaxially on *c*-Al_2O_3. This likely occurs due to lower surface energetics during growth compared to previous reports of donor-doped CdO. Lower surface energetics is a result of lower deposition temperature (200°C) compared to typical 350-400°C used in previous work [4] [5] [6] [7] on high mobility CdO, including a report on Y:CdO [9] also grown on *c*-Al_2O_3.

The non-epitaxial nature of Gd:CdO growth on *c*-Al_2O_3 may be furthered due to strain induced by the Gd dopant in the lattice. A θ-2θ scan of In:CdO grown on *c*-Al_2O_3 exhibits a much lower intensity CdO (111) peak (Figure S10b) as compared to Gd:CdO due to the film growing mostly in the <025> direction, which cannot be detected in this symmetric scan. The In:CdO is likely more susceptible to epitaxial growth due to In acting as a surfactant during growth, causing longer surface diffusion lengths such that adatoms adhere to more preferential sites and the film quality is enhanced. This phenomenon is discussed in Refs [4] [10].

CdO grown on (100) Si is not lattice matched to the substrate, resulting in polycrystalline films as shown in Figure S11c. Although films discussed in this report are not grown epitaxial to the substrates, structural defects caused by this do not significantly limit the mobility in CdO. This is because CdO has a high propensity for native oxygen vacancy formation and these defects are the dominant scattering mechanism in these films. Previous reports [4] [9] [11] have demonstrated that even as out-of-plane mosaicity in CdO increases with doping concentration, high mobility remains, suggesting that structural defects do not contribute greatly to mobility.

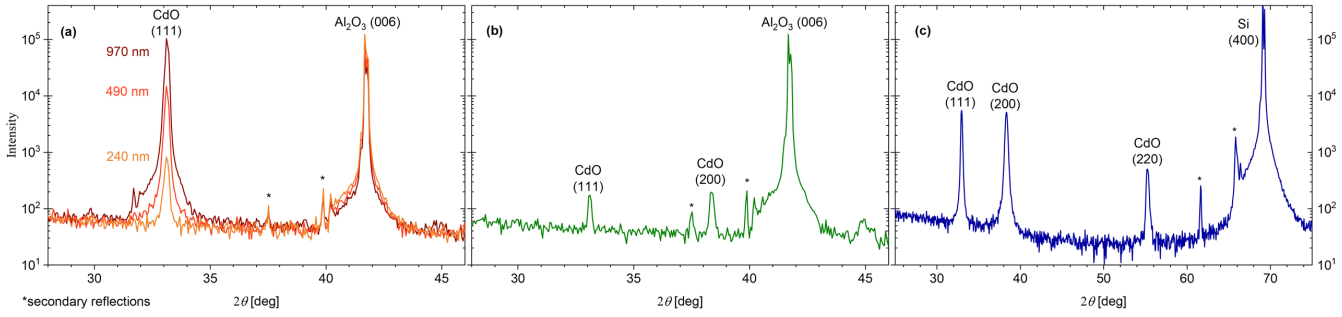

Figure S11. θ − 2θ XRD patterns for (a) Gd:CdO and (b) In:CdO grown on c-plane Al_2O_3, and (c) Gd:CdO on (100) Si.

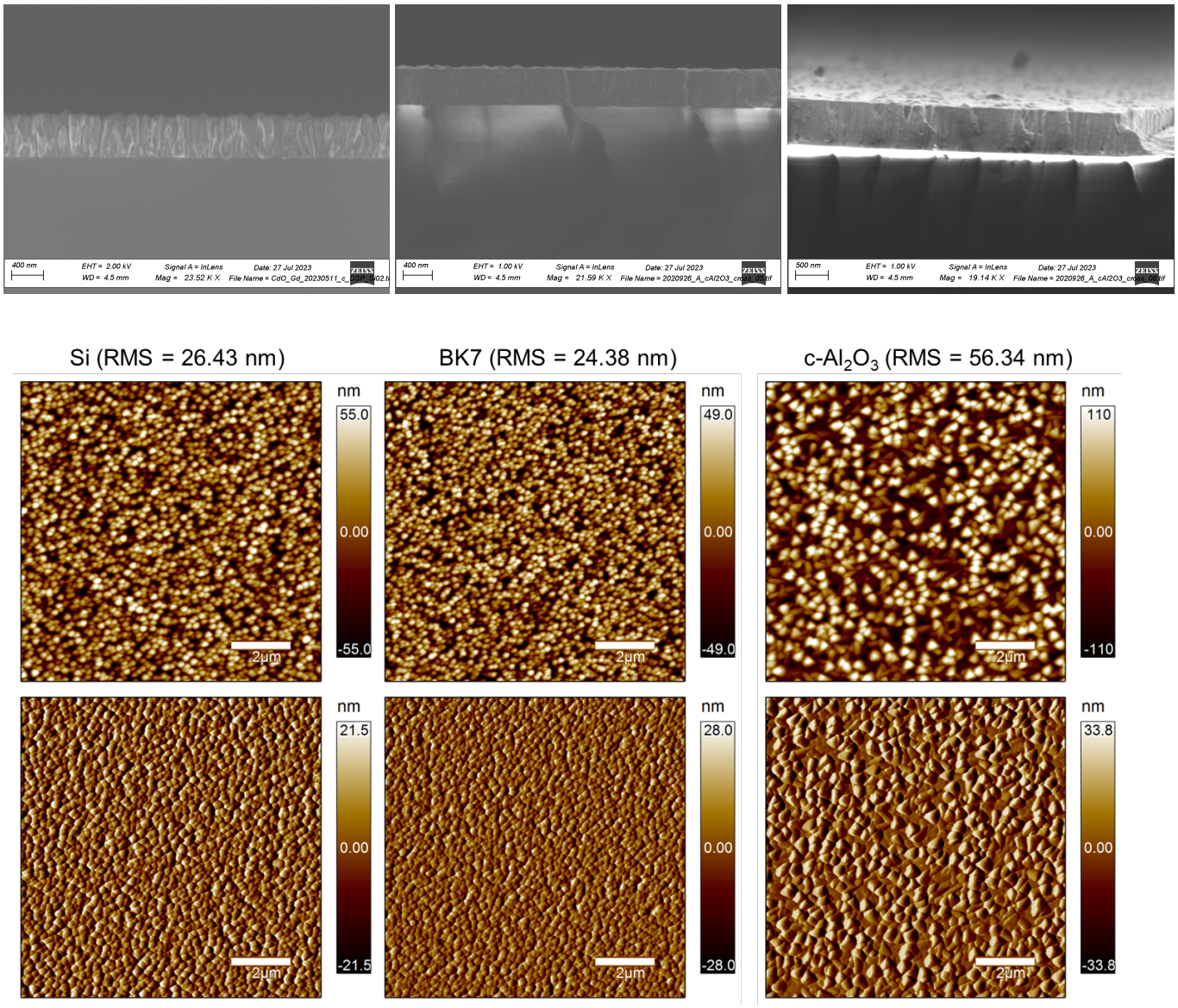

Figure S12. Cross-sectional SEM images of 500 nm thick CdO films highly doped with Gd grown on **(a)** undoped Si **(b,c)** c-plane sapphire. AFM surface map of 1 μm thick CdO films highly doped with Gd on **(d)** Si, **(e)** BK7 glass, and **(f)** c-plane sapphire. The top row images are height traces and the bottom row images are amplitude traces.

S8. Derivation of Drude permittivity tensor in a magnetic field

The goal is to derive the permittivity tensor as a function of frequency $\boldsymbol{\varepsilon}(\omega)$ of an isotropic Drude-like material in a static and uniform magnetic field $\boldsymbol{B}$, oriented in the $+z$ direction. A time varying electric field $\boldsymbol{E(t)}$ is incident on a slab of material oriented in the xy plane which perturbs electrons in the slab. Each electron can be represented as a cloud of total charge $-e$, which is perturbed from its equilibrium position by $\boldsymbol{r} \equiv x\hat{x} + y\hat{y} + z\hat{z}$ (shown in Figure S13).

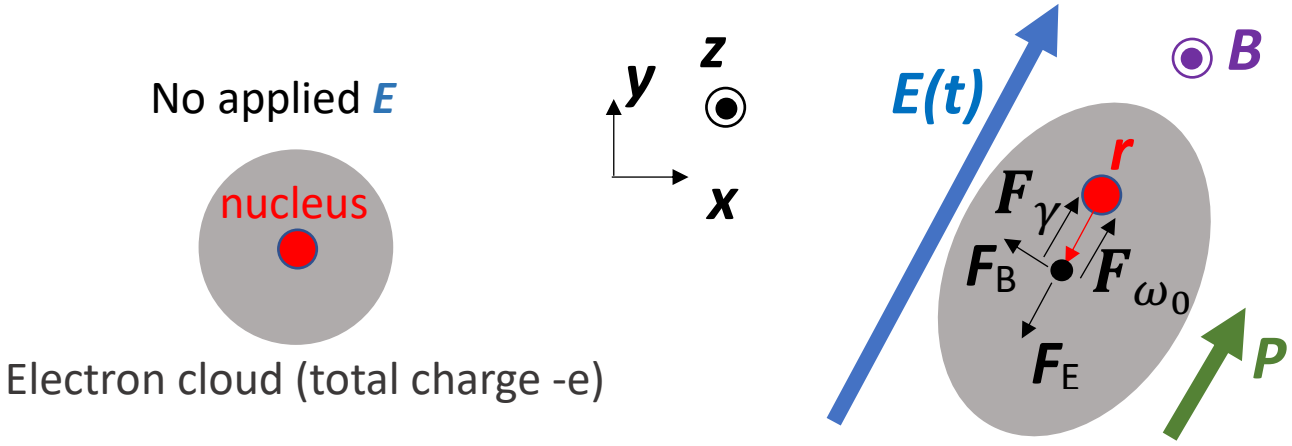

Figure S13. Free-body diagram of an electron cloud in an electric $\boldsymbol{E}$ and magnetic $\boldsymbol{B}$ field. The perturbation leads to a net polarization $\boldsymbol{P}$ in the material, which can define the frequency dependent permittivity function $\boldsymbol{\varepsilon}(\omega)$.

Starting with Newton's 2nd law, the equations of motion for the atomic nuclei relative to the center of mass for their electron cloud, which behaves like a spring system with effective mass m^*. This gives the following equations in the x, y, and z directions,

$$\sum F_x = m^* \frac{\partial^2 x}{\partial t^2} = -eE_x - m^*\gamma \frac{\partial x}{\partial t} - e\frac{\partial y}{\partial t}B - m^*\omega_0^2 x \tag{S1}$$

$$\sum F_y = m^* \frac{\partial^2 y}{\partial t^2} = -eE_y - m^*\gamma \frac{\partial y}{\partial t} + e\frac{\partial x}{\partial t}B - m^*\omega_0^2 y \tag{S2}$$

$$\sum F_z = m^* \frac{\partial^2 z}{\partial t^2} = -eE_z - m^* \gamma \frac{\partial z}{\partial t} - m^* \omega_0^2 z \tag{S3}$$

where like in the standard Lorentz model, γ represents the damping rate and the force ($\boldsymbol{F}_\gamma$) is a friction force. The term with ω_0^2 represents the restoring force ($\boldsymbol{F}_{\omega 0}$), which for the standard Drude and this model is assumed to be 0. The magnetic force term (i.e. the Lorentz force; $\boldsymbol{F}_B$) only occurs in the *xy* plane, with the *x* component of the force depending on the *y* component of the velocity and vice versa.

To clarify the origin of the sign for each term in Eqns. S1-S3, $\boldsymbol{F}_\gamma$ is a friction force, so $F_{\gamma,x}$ is negative when $\frac{\partial x}{\partial t}$ is positive, $F_{\gamma,y}$ is negative when $\frac{\partial y}{\partial t}$ is positive, and $F_{\gamma,z}$ is negative when $\frac{\partial z}{\partial t}$ is positive. Likewise, given $\boldsymbol{F}_{\omega 0}$ is a restoring force, the *x*,*y*, and *z* components' sign is opposite the sign of *x*,*y*,*z*, hence the negative sign. The Lorentz force $\boldsymbol{F}_B$ resulting from the magnetic field in the $+\hat{z}$ direction causes electrons to move counterclockwise in a circle. This means that when $\frac{\partial y}{\partial t}$ is positive, $\boldsymbol{F}_{B,x}$ is in the $-\hat{x}$ direction. However, when $\frac{\partial x}{\partial t}$ is positive, $\boldsymbol{F}_{B,y}$ is in the $+\hat{y}$ direction, which is what gives the Lorentz force in Equation S2 the opposite sign of Equation S1.

Rearranging and performing a Fourier transform $\frac{\partial^n p(t)}{\partial t^n} \rightarrow (-i\omega)^n p(\omega)$ to change from the time to frequency domain will change ***E(t)*** into ***E(ω)***, and allow *x*(*t*), *y*(*t*), and *z*(*t*) to be found as functions of frequency *x*(*ω*), *y*(*ω*), and *z*(*ω*). This turns Equations S1-S3 into:

$$eE_x = m^* \omega^2 x + i m^* \gamma \omega x + i m^* \omega_c \omega y \tag{S4}$$

$$eE_y = m^* \omega^2 y + i m^* \gamma \omega y - i m^* \omega_c \omega x \tag{S5}$$

$$eE_z = m^* \omega^2 z + i m^* \gamma \omega z\,, \tag{S6}$$

where the cyclotron frequency is defined as $\omega_c \equiv \frac{eB}{m^*}$. Solving for $x(\omega)$, $y(\omega)$, and $z(\omega)$ gives:

$$x = \frac{eE_x - i\, m^* \omega_c \omega y}{m^* \omega(\omega + i\gamma)} \tag{S7}$$

$$y = \frac{eE_y + i\, m^* \omega_c \omega x}{m^* \omega(\omega + i\gamma)} \tag{S8}$$

$$z = \frac{eE_z}{m^* \omega(\omega + i\gamma)}, \tag{S9}$$

where $x(\omega)$, $y(\omega)$ depend on each other. Inserting Equation S8 into Equation S7 and simplifying to solve for x, and Equation S7 into Equation S8 and simplifying to solve for y gives:

$$x = \frac{e}{m^* \omega} \frac{\left[(\omega + i\gamma)E_x - i\, \omega_c E_y\right]}{\left[(\omega + i\gamma)^2 - \omega_c^2\right]} \tag{S10}$$

$$y = \frac{e}{m^* \omega} \frac{\left[i\, \omega_c E_x + (\omega + i\gamma)E_y\right]}{\left[(\omega + i\gamma)^2 - \omega_c^2\right]}. \tag{S11}$$

We can define the dipole moment $\boldsymbol{\mu}$ of the system as $\boldsymbol{\mu} \equiv -\mathrm{e}\boldsymbol{r}$. Breaking $\boldsymbol{\mu}$ into components and inserting Equations S9-S11 gives:

$$\mu_x = \frac{-e^2}{m^* \omega} \frac{\left[(\omega + i\gamma)E_x - i\, \omega_c E_y\right]}{\left[(\omega + i\gamma)^2 - \omega_c^2\right]} \tag{S12}$$

$$\mu_y = \frac{-e^2}{m^* \omega} \frac{\left[i\, \omega_c E_x + (\omega + i\gamma)E_y\right]}{\left[(\omega + i\gamma)^2 - \omega_c^2\right]} \tag{S13}$$

$$\mu_z = \frac{-e^2 E_z}{m^* \omega(\omega + i\gamma)}. \tag{S14}$$

We can define the polarizability tensor $\boldsymbol{\alpha}$ as being $\boldsymbol{\mu} \equiv \boldsymbol{\alpha}\boldsymbol{E}$, or

$$\begin{bmatrix} \mu_x \\ \mu_y \\ \mu_z \end{bmatrix} \equiv \begin{bmatrix} \alpha_{xx} & \alpha_{xy} & \alpha_{xz} \\ \alpha_{yx} & \alpha_{yy} & \alpha_{yz} \\ \alpha_{zx} & \alpha_{zy} & \alpha_{zz} \end{bmatrix} \begin{bmatrix} E_x \\ E_y \\ E_z \end{bmatrix}, \tag{S15}$$

which can also be written as:

$$\mu_x = \alpha_{xx}E_x + \alpha_{xy}E_y + \alpha_{xz}E_z \tag{S16}$$

$$\mu_y = \alpha_{yx}E_x + \alpha_{yy}E_y + \alpha_{yz}E_z \tag{S17}$$

$$\mu_z = \alpha_{zx}E_x + \alpha_{zy}E_y + \alpha_{zz}E_z\,. \tag{S18}$$

To find each term of the polarizability tensor, we term match Equations S12-S14 with Equations S16-S18 giving:

$$\alpha_{xx} = \alpha_{yy} = \frac{-e^2}{m^*\omega}\frac{(\omega + i\gamma)}{[(\omega + i\gamma)^2 - \omega_c^2]} \tag{S19}$$

$$\alpha_{xy} = -\alpha_{yx} = \frac{e^2}{m^*\omega}\frac{i\omega_c}{[(\omega + i\gamma)^2 - \omega_c^2]} \tag{S20}$$

$$\alpha_{zz} = \frac{-e^2}{m^*\omega(\omega + i\gamma)} \tag{S21}$$

$$\alpha_{zx} = \alpha_{zy} = \alpha_{xz} = \alpha_{yz} = 0\,. \tag{S22}$$

The induced polarization in the material $\boldsymbol{P}$ is defined as the sum of all N dipole moments created by the applied electric field per unit volume. The (linear) electric susceptibility tensor $\boldsymbol{\chi}$ can then be defined from the polarization; $\boldsymbol{P} = \frac{1}{V}\sum_{\boldsymbol{V}} \mu_i = N\boldsymbol{\mu} = N\boldsymbol{\alpha}\boldsymbol{E} \equiv \varepsilon_0\boldsymbol{\chi}\boldsymbol{E}$, written out as:

$$\begin{bmatrix} P_x \\ P_y \\ P_z \end{bmatrix} = N\begin{bmatrix} \langle\mu_x\rangle \\ \langle\mu_y\rangle \\ \langle\mu_z\rangle \end{bmatrix} = N\begin{bmatrix} \alpha_{xx} & \alpha_{xy} & \alpha_{xz} \\ \alpha_{yx} & \alpha_{yy} & \alpha_{yz} \\ \alpha_{zx} & \alpha_{zy} & \alpha_{zz} \end{bmatrix}\begin{bmatrix} E_x \\ E_y \\ E_z \end{bmatrix} \equiv \varepsilon_0\begin{bmatrix} \chi_{xx} & \chi_{xy} & \chi_{xz} \\ \chi_{yx} & \chi_{yy} & \chi_{yz} \\ \chi_{zx} & \chi_{zy} & \chi_{zz} \end{bmatrix}\begin{bmatrix} E_x \\ E_y \\ E_z \end{bmatrix}, \tag{S23}$$

where ε_0 is the permittivity of free space. Simplifying and term matching each component of $\boldsymbol{\chi}$ to $\boldsymbol{\alpha}$ gives:

$$\chi_{xx} = \chi_{yy} = \frac{-\omega_p^2(\omega + i\gamma)}{\omega[(\omega + i\gamma)^2 - \omega_c^2]} \tag{S24}$$

$$\chi_{xy} = -\chi_{yx} = \frac{i\omega_p^2\omega_c}{\omega[(\omega + i\gamma)^2 - \omega_c^2]} \tag{S25}$$

$$\chi_{zz} = \frac{-\omega_p^2}{\omega(\omega + i\gamma)} \tag{S26}$$

$$\chi_{xz} = \chi_{yz} = \chi_{zx} = \chi_{zy} = 0\,, \tag{S27}$$

where the plasma frequency is defined as $\omega_p \equiv \sqrt{\frac{Ne^2}{m^*\varepsilon_0}}$. The displacement field $\boldsymbol{D}$ and permittivity tensor $\boldsymbol{\varepsilon}$ can be defined as $\boldsymbol{D} \equiv \boldsymbol{\varepsilon_0 E} + \boldsymbol{P} = \boldsymbol{\varepsilon_0 E} + \boldsymbol{\varepsilon_0 \chi E} \equiv \boldsymbol{\varepsilon_0 \varepsilon_r E} \equiv \boldsymbol{\varepsilon E}$. Thus, we have a relation between $\boldsymbol{\chi}$ and $\boldsymbol{\varepsilon}$, where $\boldsymbol{\varepsilon} = \varepsilon_0(1 + \boldsymbol{\chi})$. However, in the optical range of frequencies we are interested in, there are still higher frequency contributions to the permittivity which manifest as a DC offset to the permittivity (the high frequency permittivity ε_∞). Because ε_∞ comes from contributions of the isotropic material it is assumed to be the same in each direction, and 0 for the off-diagonal components (otherwise the material would naturally have off diagonal components, which is not true for an isotropic material). For modeling in the optical frequency bandwidth of interest, a better representation of the permittivity is therefore:

$$\boldsymbol{\varepsilon} = \varepsilon_0(\boldsymbol{\varepsilon}_\infty + \boldsymbol{\chi}) = \varepsilon_0\begin{pmatrix} \varepsilon_\infty + \chi_{xx} & \chi_{xy} & \chi_{xz} \\ \chi_{yx} & \varepsilon_\infty + \chi_{yy} & \chi_{yz} \\ \chi_{zx} & \chi_{zy} & \varepsilon_\infty + \chi_{zz} \end{pmatrix} = \varepsilon_0\begin{pmatrix} \varepsilon_{xx} & \varepsilon_{xy} & \varepsilon_{xz} \\ \varepsilon_{yx} & \varepsilon_{yy} & \varepsilon_{yz} \\ \varepsilon_{zx} & \varepsilon_{zy} & \varepsilon_{zz} \end{pmatrix}. \tag{S28}$$

Term matching $\boldsymbol{\chi}$ to $\boldsymbol{\varepsilon}$, we find our final equations for the permittivity tensor as a function of frequency:

$$\varepsilon_{xx} = \varepsilon_{yy} = \varepsilon_{\infty} - \frac{\omega_p^2(\omega + i\gamma)}{\omega[(\omega + i\gamma)^2 - \omega_c^2]} \tag{S29}$$

$$\varepsilon_{xy} = -\varepsilon_{yx} = \frac{i\omega_p^2\omega_c}{\omega[(\omega + i\gamma)^2 - \omega_c^2]} \tag{S30}$$

$$\varepsilon_{zz} = \varepsilon_{\infty} - \frac{\omega_p^2}{\omega(\omega + i\gamma)} \tag{S31}$$

$$\varepsilon_{xz} = \varepsilon_{yz} = \varepsilon_{zx} = \varepsilon_{zy} = 0. \tag{S32}$$

It is clear from Equations S29-S32 that when the applied magnetic field is removed ($\omega_c = 0$), the permittivity tensor again resembles that of an isotropic material. As shown in the main text, it is often convenient to define $\varepsilon_{xy} \equiv -ig$;

$$g = \frac{-\omega_p^2\omega_c}{\omega[(\omega + i\gamma)^2 - \omega_c^2]}. \tag{S33}$$

In summary, an external magnetic field in the *z* direction exerts a Lorentz force in the *xy* plane which perturbs electron motion, resulting in off-diagonal terms in the permittivity tensor and additional terms in the on-diagonal components in the *x* and *y* directions. The value of ω for which $\varepsilon = 0$ in Equation S31 is known as the epsilon-near-zero (ENZ) frequency, where $\omega_{\mathrm{ENZ}} \approx \omega_{\mathrm{p}}/\sqrt{\varepsilon_{\infty}}$ if γ is small. This can be expressed as an ENZ wavelength given by $\lambda_{\mathrm{ENZ}} = 2\pi c/\omega_{\mathrm{ENZ}}$, where c and λ are the vacuum speed and wavelength of light respectively.

S9. MO polarimeter measurement setup

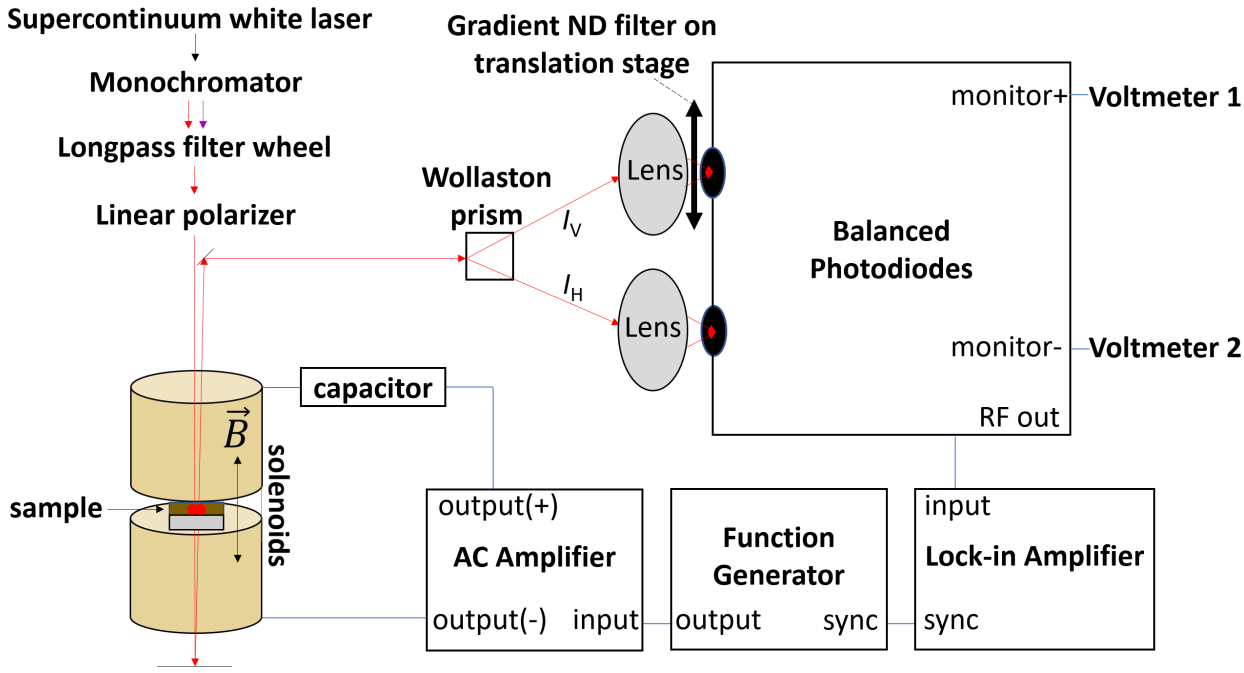

Figure S14. Diagram of the MO polarimeter used to measure Faraday rotation. A Wollaston prism splits the linearly polarized light into its vertical (I_V) and horizontal (I_H) components, which slightly vary in magnitude as the light is Faraday rotated as it passes through the sample in an AC magnetic field.

Supplementary References

[1] A. R. Taussig, G. F. Dionne and C. A. Ross, "Dependence of Faraday rotation and magneto-optical figure of merit on dielectric tensor elements in materials with uniaxial symmetry," *Physical Review B,* vol. 77, p. 012407, 2008.

[2] N. Peard, D. Callahan, J. C. Perkinson, Q. Du, N. S. Patel, T. Fakhrul, J. LeBlanc, C. A. Ross, J. Hu and C. Y. Wang, "Magneto-optical properties of InSb for infrared spectral filtering," *Journal of Applied Physics,* vol. 129, p. 203104, 2021.

[3] J. R. Nolen, E. L. Runnerstrom, K. P. Kelley, T. S. Luk, T. G. Folland, A. Cleri, J.-P. Maria and J. D. Caldwell, "Ultraviolet to far-infrared dielectric function of n-doped cadmium oxide thin films," *Physical Review Materials,* vol. 4, p. 025202, 2020.

[4] A. Cleri, J. Tomko, K. Quiambao-Tomko, M. V. Imperatore, Y. Zhu, J. R. Nolen, J. Nordlander, J. D. Caldwell, Z. Mao, N. C. Giebink and others, "Mid-wave to near-IR optoelectronic properties and epsilon-near-zero behavior in indium-doped cadmium oxide," *Physical Review Materials,* vol. 5, p. 035202, 2021.

[5] A. J. Cleri, J. R. Nolen, K. G. Wirth, M. He, E. L. Runnerstrom, K. P. Kelley, J. Nordlander, T. Taubner, T. G. Folland, J.-P. Maria and others, "Tunable, Homoepitaxial Hyperbolic Metamaterials Enabled by High Mobility CdO," *Advanced optical materials,* vol. 11, p. 2202137, 2023.

[6] K. P. Kelley, E. L. Runnerstrom, E. Sachet, C. T. Shelton, E. D. Grimley, A. Klump, J. M. LeBeau, Z. Sitar, J. Y. Suen, W. J. Padilla and others, "Multiple epsilon-near-zero resonances in multilayered cadmium oxide: designing metamaterial-like optical properties in monolithic materials," *Acs Photonics,* vol. 6, p. 1139–1145, 2019.

[7] E. Sachet, C. T. Shelton, J. S. Harris, B. E. Gaddy, D. L. Irving, S. Curtarolo, B. F. Donovan, P. E. Hopkins, P. A. Sharma, A. L. Sharma and others, "Dysprosium-doped cadmium oxide as a gateway material for mid-infrared plasmonics," *Nature materials,* vol. 14, p. 414–420, 2015.

[8] E. L. Runnerstrom, K. P. Kelley, T. G. Folland, J. R. Nolen, N. Engheta, J. D. Caldwell and J.-P. Maria, "Polaritonic hybrid-epsilon-near-zero modes: beating the plasmonic confinement vs propagation-length trade-off with doped cadmium oxide bilayers," *Nano letters,* vol. 19, p. 948–957, 2018.

[9] K. P. Kelley, E. Sachet, C. T. Shelton and J.-P. Maria, "High mobility yttrium doped cadmium oxide thin films," *APL Materials,* vol. 5, p. 076105, 2017.

[10] M. Baldini, M. Albrecht, D. Gogova, R. Schewski and G. Wagner, "Effect of indium as a surfactant in (Ga1- xInx) 2O3 epitaxial growth on β-Ga2O3 by metal organic vapour phase epitaxy," *Semiconductor Science and Technology,* vol. 30, p. 024013, 2015.

[11] E. L. Runnerstrom, K. P. Kelley, E. Sachet, C. T. Shelton and J.-P. Maria, "Epsilon-near-zero modes and surface plasmon resonance in fluorine-doped cadmium oxide thin films," *ACS Photonics,* vol. 4, p. 1885–1892, 2017.